Relativistic numerical model for close neutron-star binaries

J. R. Wilson
University of California, Lawrence Livermore National Laboratory, Livermore, California 94550

G. J. Mathews and P. Marronetti
University of Notre Dame, Department of Physics, Notre Dame, Indiana 46556

(Received 21 December 1995)

We describe a numerical method for calculating the (3+1)-dimensional general relativistic hydrodynamics of a coalescing neutron-star binary system. The relativistic field equations are solved at each time slice with a spatial three-metric chosen to be conformally flat. Against this solution to the general relativistic field equations, the hydrodynamic variables and gravitational radiation are allowed to respond. The gravitational radiation signal is derived via a multipole expansion of the metric perturbation to the hexadecapole ($l=4$) order including both mass and current moments and a correction for the slow-motion approximation. Using this expansion, the effect of gravitational radiation on the system evolution can also be recovered by introducing an acceleration term in the matter evolution. In the present work we illustrate the method by applying this model to evaluate various orbits of two neutron stars with a gravitational mass of $1.45M_{\odot}$ near the time of the final merger. We discuss the evidence that, for a realistic neutron-star equation of state, general relativistic effects may cause the stars to individually collapse into black holes prior to merging. Also, the strong fields cause the last stable orbit to occur at a larger separation distance and lower frequency than previously estimated. [S0556-2821(96)01412-9]

PACS number(s): 98.80.Fk, 04.25.Dm, 04.30.Db, 04.40.Dg

I. INTRODUCTION

Coalescing neutron stars are currently of interest for a number of reasons. Several neutron-star binaries are known to exist in the Galaxy (e.g., PSR 1913+16 [1], PSR 2303+46 [2], PSR 2127+11C [3], PSR 1534+11 [4]) whose orbits are observed to decay on a time scale of $1-3\times10^8$ yr. It has been recognized for some time [5–10] that the final stages of coalescence of such systems could be copious producers of gravitational radiation. This possibility has recently received renewed interest with the development of next generation gravity-wave detectors such as cryogenic bar detectors [11], the Caltech-MIT Laser Interferometric Gravitational Wave Observatory (LIGO) detector [12], and its European counterparts, GEO and VIRGO (e.g., [13]) for which an event rate due to binary neutron-star coalescence out to 200 Mpc could be $\gtrsim 3$ per yr [6,14,15]. It has also been proposed that such events (when integrated over the number of galaxies out to high redshifts) could account for the observed event rate and energy requirements of γ-ray bursts [16–18]. Coalescing neutron stars might even be significant contributors to heavy element nucleosynthesis in the Galaxy [19,20].

For much of the evolution of a neutron-star binary, the system should be amenable to a point source description using post-Newtonian techniques [21–23]. However, as the stars approach one another the gravitational fields become quite strong and hydrodynamic effects should become significant. Indeed, it is expected that the wave forms could become quite complex as the stars merge. This complexity, however, may be sensitive to various physical properties of the coalescing system [10] such as the neutron-star equation of state (EOS). Hence, careful modeling is needed which includes both the nonlinear general relativistic effects and a realistic neutron-star equation of state. Such calculations can be used as a foundation for extraction of the information contained in the detected gravity waves and as a framework in which to analyze possible γ-ray burst models.

A computation of the hydrodynamic evolution is complicated, however, due to the inherently three-dimensional character of the orbiting system. To this end several attempts have been made to model the hydrodynamics of coalescence in either a Lagrangian smoothed-particle Newtonian approximation [24,25] or using conventional finite-difference methods in the post-Newtonian approximation [26–29]. It is important to appreciate, however, that as the two neutron stars coalesce the system becomes strongly relativistic, and the validity of Newtonian or post-Newtonian hydrodynamics may be questionable. In the present work, therefore, we improve upon such calculations in that we explicitly include most of the effects of a fully general relativistic treatment.

Some preliminary discussion of this work has been reported previously [30–35]. In this paper we present detailed discussion of our method of solving the relativistic field equations and hydrodynamics. As an illustration and for comparison with existing calculations in the literature, we present orbit calculations for two neutron stars with a gravitational mass of $1.45M_{\odot}$ each. We find that the last stable orbit occurs for a separation distance ≈ 1.4 times larger and a frequency smaller than those estimated using the post-Newtonian approximation. We also find the surprising result that with a realistic equation of state, the strong fields may induce otherwise stable neutron stars to collapse into black holes prior to orbit instability and merging.

II. THE MODEL

A. Coordinate system

We start with the usual slicing of spacetime into a one-parameter family of hypersurfaces separated by differential displacements in timelike coordinates as defined in the Arnowitt-Deser-Misner (ADM) or (3+1) formalism [36,37].

For this work we have considered a number of possible three-space coordinate systems, e.g., polar, bipolar, spherical, cylindrical. Ultimately, we have selected Cartesian x,y,z isotropic coordinates. This is a natural coordinate system for three-dimensional problems, in that no special point or singularity is introduced. It thus avoids problems associated with finite differencing near coordinate singularities. It also has the advantage that the relativistic field equations assume a simpler and more symmetric form.

With this choice for coordinates, proper distance is expressed

$$ds^2 = -(\alpha^2 - \beta_i\beta^i)dt^2 + 2\beta_i dx^i dt + \gamma_{ij}dx^i dx^j, \qquad (1)$$

where the lapse function α is a multiplier which describes the differential lapse of proper time between two hypersurfaces. In the Newtonian limit this quantity approaches unity and is related to the Newtonian gravitational potential. The quantity β_i is the shift vector denoting the shift in spacelike coordinates between hypersurfaces. The quantity γ_{jk} is the metric of the three-geometry. It specifies the distance between points within a hypersurface.

Here, we introduce an approximation that the three-geometry is both conformal and flat. That is, we write,

$$\gamma_{ij} = \phi^4 \hat{\gamma}_{ij}, \qquad (2)$$

and

$$\hat{\gamma}_{ij} = \delta_{ij}, \qquad (3)$$

where the conformal factor ϕ is a positive scalar function describing the ratio between the scale of distance in the curved space relative to our flat space manifold, and δ_{jk} is the Kronecker delta. This is an approximate gauge condition which we will henceforth refer to as *the conformally flat condition* (CFC). This approximation is motivated both by the general observation that gravitational radiation in most systems studied so far is small [38,39], and the fact that conformal flatness on each spacelike slice considerably simplifies the solution to the field equations.

To see the way in which the CFC allows us to solve the relativistic field equations, consider the exact equation [40]

$$\dot{\gamma}_{ij} = -2\alpha K_{ij} + D_i\beta_j + D_j\beta_i, \qquad (4)$$

where D_i is the three-space covariant derivative [40], and K_{ab} is the extrinsic curvature describing the deformation of a figure as it is carried forward by one unit in proper time in a direction normal to a hypersurface.

Equation (4) is well approximated by a conformal representation (2) *only if* the trace-free part of the right-hand side (RHS) vanishes. Thus, a spatially flat three-metric requires

$$2\alpha K_{ij} = \left(D_i\beta_j + D_j\beta_i - \frac{2}{3}\gamma_{ij}D_k\beta^k \right), \qquad (5)$$

where we have also employed the maximal slicing condition $\mathrm{tr}(K_{ab}) = 0$ as a gauge choice.

We use Eq. (5) to determine the extrinsic curvature. A convenient consequence of this is that any geometry which is initially conformally flat, will remain conformally flat to the extent that energy in gravitational radiation is unimportant. Equation (5) allows us to derive constraint equations for the lapse function and conformal factor as described in the next section.

As a final condition, we take the coordinate system to be rotating in such a way as to minimize the matter motion in the coordinate grid. This condition enhances the stability of the computation of the hydrodynamic evolution. However, this is a nontrivial condition to impose in curved spacetime which we achieve by boundary conditions on β^i as described below. All relevant forces are computed first in nonrotating coordinates which are then transformed to update the matter fields in a rotating grid.

B. General relativistic field equations

For most gravitating systems studied so far (e.g., [38,39]), only a relatively small amount of energy is emitted by gravitational waves. Even for the merger of two black holes it is expected [39] that only a few tenths of a percent of the rest mass will be radiated away in gravitation. For the case of two neutron stars we would not expect any more radiation to be emitted during the last few orbits than that for a two black-hole merger, i.e., during the inspiral, the radiated energy per orbit is a minuscule fraction of the energy in orbital motion. Furthermore, an explicit treatment of the radiation reaction is exceedingly difficult [38]. To treat the effects of gravitational waves we use a multipole formalism [37,41]. We use a radiation reaction potential in the hydrodynamics equations to account for the effect of gravity waves on the system.

The implementation of this approximation means that, given a distribution of mass and momentum on some manifold, we first solve the constraint equations of general relativity (GR) at each time in the calculation for a fixed distribution of matter. Then, we let the matter and gravitational radiation respond to this geometry. That is, we evolve the hydrodynamic equations to the next time step under an assumption of ''instantaneous gravity.'' However, at each time step we obtain a time symmetric solution to the field equations.

As an alternative to the explicit coupling of emitted gravitational radiation to the hydrodynamic and geometric evolutions of the system, the initial evolution of the system (while the gravitational radiation is a small perturbation) can be approximated by stable orbits in the absence of energy and momentum loss due to gravitational radiation. One can then (after the fact) compute the expected gradual loss rates of energy and momentum in gravity waves. This latter approach is applied in some illustrative calculation presented here. In a future paper we will apply the former method to describe the late time merging and coalescence.

Our basic approach to a solution to the GR equations is to reduce all of the constraint equations to effective flat-space elliptic equations which are amenable to standard techniques. In what follows we make use of the usual natural units in

which $G=c=1$. Thus, at each time slice we can obtain a numerically valid static solution to the exact GR field equations and information on the hydrodynamic evolution and generation of gravitational radiation. However, the advance from one time slice to the next incorporates the approximation that the effects of gravitational radiation can be described using a multipole expansion.

1. Hamiltonian constraint

We begin with the Hamiltonian constraint equation [40]. We use the forms of equations as given by Evans [38]. We show here that the Hamiltonian constraint and the maximal slicing condition $[\mathrm{tr}(K)=0]$ can be combined so as to form elliptic equations for both the conformal factor ϕ and the product $(\alpha\phi)$.

The Hamiltonian constraint equation can be written

$$R=16\pi\rho_H+K_{ij}K^{ij}-K^2, \tag{6}$$

where R is the Ricci scalar curvature, and

$$\rho_H=\rho hW^2-P, \tag{7}$$

where ρ is the proper baryonic matter density, W is the generalization of the special relativistic γ factor ($W=\alpha U^t$, where U^μ is the four-velocity), P is the pressure, and h is the specific relativistic enthalpy,

$$h=1+\epsilon+P/\rho, \tag{8}$$

with ϵ the associated matter energy above the baryon rest energy, and P the matter pressure.

The conformal scaling of the three-metric, Eq. (2), defines a conformal metric and manifold $(\hat{\gamma},\hat{M})$ related to the physical metric and manifold (γ,M) (see Refs. [40,38]). Covariant derivatives D_i and $\hat{D}_i$ on M and $\hat{M}$ can be related by calculating the transformation of the Christoffel connections:

$$\Gamma^i_{jk}=\hat{\Gamma}^i_{jk}+2\phi^{-1}[\delta^i_j\hat{D}_k\phi+\delta^i_k\hat{D}_j\phi-\hat{\gamma}_{jk}\hat{\gamma}^{il}\hat{D}_l\phi]. \tag{9}$$

With this, the transformation of the Ricci scalar curvature is

$$R=\phi^{-4}\hat{R}-8\phi^{-5}\hat{\Delta}\phi, \tag{10}$$

where $R=R(\gamma)$, $\hat{R}=\hat{R}(\hat{\gamma})$, and $\hat{\Delta}=\hat{\gamma}^{ij}\hat{D}_i\hat{D}_j$. As mentioned in Sec. II A, we choose a conformally flat metric, $\hat{\gamma}^{ij}=\delta^{ij}$, for which $\hat{\Gamma}^i_{jk}\to 0$, $\hat{D}_i\to\nabla$, $\hat{R}\to 0$, and $\hat{\Delta}\to\nabla^2$, the flat-space Laplacian.

Solving Eq. (10) for $\hat{\Delta}\phi$, and combining with the Hamiltonian constraint gives the desired form for an elliptic equation for ϕ:

$$\nabla^2\phi=-\frac{\phi^5}{8}[16\pi\rho_H+K_{ij}K^{ij}]. \tag{11}$$

In order to put this constraint equation into a form which is useful for a solution along with the hydrodynamic variables, we must introduce conformal scalings for the source terms. To do this, the equation of state is introduced through the adiabatic index Γ:

$$P=(\Gamma-1)\rho\epsilon, \tag{12}$$

where Γ is a function of state variable for each zone. With this equation of state, (7) becomes

$$\rho_H=\rho W^2+\rho\epsilon W\left[\Gamma W-\frac{(\Gamma-1)}{W}\right]. \tag{13}$$

For the hydrodynamic Lorentz contracted density, $D=\rho W$ and energy $E=\rho\epsilon W$, we introduce the conformal scalings

$$D=\phi^{-6}\hat{D}, \tag{14}$$

$$E=\phi^{-6\Gamma}\hat{E}. \tag{15}$$

The reasons for these choices will be made clear when we consider the hydrodynamic equations given in Sec. II C.

The extrinsic curvature is scaled by

$$K^{ij}=\phi^{-10}\hat{K}^{ij}, \tag{16}$$

which gives

$$K_{ij}=\phi^{-2}\hat{K}_{ij}. \tag{17}$$

With the introduction of these scalings, the Hamiltonian constraint can be written into the desired form:

$$\nabla^2\phi=-\left[2\pi\hat{D}W\phi^{-1}+2\pi\hat{E}\left(\Gamma W-\frac{\Gamma-1}{W}\right)\phi^{5-6\Gamma}+\frac{1}{8}\hat{K}_{ij}\hat{K}^{ij}\phi^{-7}\right]. \tag{18}$$

This can be written in a more familiar Poisson form:

$$\nabla^2\phi=-4\pi\rho_1, \tag{19}$$

in which the source term can be identified in terms of physical hydrodynamic variables by transforming the conformal scalings in Eq. (18):

$$\rho_1=\frac{\phi^5}{2}\left[DW+E\left(\Gamma W-\frac{(\Gamma-1)}{W}\right)+\frac{1}{16\pi}K_{ij}K^{ij}\right]. \tag{20}$$

2. Lapse function

We also use the Hamiltonian constraint together with the maximal slicing condition $tr(k)=0$ to obtain an elliptic constraint equation for the lapse function α. We begin with the identities

$$\Delta\alpha=\Delta[\phi^{-1}(\alpha\phi)]=D_iD^i[\phi^{-1}(\alpha\phi)] \tag{21}$$

$$=\phi^{-1}\Delta(\alpha\phi)-2\phi^{-6}\hat{\gamma}^{ij}\hat{D}_i\phi\hat{D}_j(\alpha\phi)+\alpha\phi\Delta(\phi^{-1}). \tag{22}$$

Now, in our conformally flat metric, one can write, for any scalar function, and, in particular, for the quantity $(\alpha\phi)$,

$$\Delta(\alpha\phi)=\phi^{-4}\hat{\Delta}(\alpha\phi)+2\phi^{-5}\hat{\gamma}^{ij}(\hat{D}_i\phi)[\hat{D}_j(\alpha\phi)]. \tag{23}$$

Substituting this into Eq. (22) gives

$$\Delta\alpha=\phi^{-5}\hat{\Delta}(\alpha\phi)+\alpha\phi\Delta(\phi^{-1}). \tag{24}$$

Now, from the transformation properties of the Ricci curvature scalar (10), Eq. (24) can be rearranged as

$$\hat{\Delta}(\alpha\phi)=\phi^5\Delta\alpha+\tfrac{1}{8}\,\alpha\phi^5[\hat{R}\phi^{-4}-R]. \tag{25}$$

Rewriting the Hamiltonian constraint (6) to include the CFC and maximal slicing conditions, then leads to a flat-space elliptic equation in $(\alpha\phi)$:

$$\nabla^2(\alpha\phi)=\tfrac{1}{8}\,\alpha\phi^5[16\pi\rho(3W^2-2)+16\pi\rho\epsilon[3\Gamma(W^2+1)-5]+7K_{ij}K^{ij}]. \tag{26}$$

In Poisson-like form this is

$$\nabla^2(\alpha\phi)=4\pi\rho_2, \tag{27}$$

with the source term written in terms of hydrodynamic variables as

$$\rho_2=\frac{\alpha\phi^5}{2}\left[\frac{D(3W^2-2)+E[3\Gamma(W^2+1)-5]}{W}+\frac{7}{16\pi}K_{ij}K^{ij}\right]. \tag{28}$$

A solution of equation (27) determines the lapse function after Eq. (19) is used to determine the conformal factor.

3. Momentum constraint

With the lapse function and conformal factor determined from the Hamiltonian constraint and maximal slicing condition, we then use the momentum constraints to find the shift vector.

The momentum constraints have the form [38],

$$D_i(K^{ij}-\gamma^{ij}K)=8\pi S^j, \tag{29}$$

where D_j is the three-space covariant derivative [40]. S^i is the contravariant material momentum density which is derived from the solution to the hydrodynamic equations, Sec. II C. In our maximal-slicing conformally flat conditions, the second term on the left-hand side (LHS) of Eq. (29) vanishes and we have

$$D_iK^{ij}=8\pi S^j. \tag{30}$$

Using (17) and (9), it can be verified that

$$D_iK^{ij}=\phi^{-10}\hat{D}_i(\phi^{10}K^{ij}). \tag{31}$$

Now converting our ''conformally flat condition'' [i.e., Eq. (5)] from covariant derivatives to $\hat{D}^a$ or ordinary derivatives, and inserting into Eq. (31), gives

$$D_iK^{ij}=\frac{\phi^{-10}}{2}\hat{D}_i\left[\frac{\phi^6}{\alpha}\left(\hat{D}^i\beta^j+\hat{D}^j\beta^i-\frac{2}{3}\,\hat{\gamma}^{ij}\hat{D}_k\beta^k\right)\right]. \tag{32}$$

Combining this with (30) then gives

$$\hat{D}_i[\hat{D}^i\beta^j+\hat{D}^j\beta^i-\tfrac{2}{3}\,\hat{\gamma}^{ij}\hat{D}_k\beta^k]=Q^j, \tag{33}$$

where the source term Q^j is defined

$$Q^j\equiv16\pi\alpha\phi^4S^j+\frac{\hat{D}_i\xi}{\xi}\left[\hat{D}^i\beta^j+\hat{D}^j\beta^i-\frac{2}{3}\,\hat{\gamma}^{ij}\hat{D}_k\beta^k\right], \tag{34}$$

where $\xi\equiv\alpha/\phi^6$.

Equation (33) can be reduced to

$$\nabla^2\beta^j=\frac{\partial}{\partial x^j}\left(\frac{1}{3}\nabla\cdot\beta\right)+Q^j. \tag{35}$$

Thus, by introducing a decomposition of β^i into

$$\beta^i=B^i-\tfrac{1}{4}\,\partial_i\chi, \tag{36}$$

the following two elliptic equations result:

$$\nabla^2\chi=\tfrac{4}{3}\,\nabla\cdot\beta, \tag{37}$$

$$\nabla^2B^i=Q^i. \tag{38}$$

These we use to determine the components of the shift vector.

This is the desired result except for the fact that most of the momentum encompassed in Eqs. (34) and (38) is simply the orbital motion of the binary. We, therefore, define a rotating coordinate system with a rotation-subtracted shift vector in which the nonorbital aspects of matter evolution and relativity (e.g., frame drag) can be more easily studied. To do this we decompose B^i into a frame-drag term G^i and an orbital motion term:

$$B^i=G^i+(\omega\times r)^i, \tag{39}$$

and subtract the orbital velocity of the coordinate system from both sides of Eq. (35). Ultimately, we write Eq. (38) in the Poisson-like form

$$\nabla^2B^i=4\pi\rho_3^i, \tag{40}$$

where

$$\rho_3^i=[4\alpha\phi^4S_i-4\beta^iW(D+\Gamma E)]+\frac{1}{4\pi\xi}\,\frac{\partial\xi}{\partial x^j}\left(\frac{\partial\beta^i}{\partial x^j}+\frac{\partial\beta^j}{\partial x^i}-\frac{2}{3}\,\delta_{ij}\frac{\partial\beta^k}{\partial x^k}\right). \tag{41}$$

Since $\nabla^2(\omega\times r)=0$, B^i and G^i can be used interchangeably in Eq. (40).

As the meaning of orbital angular velocity becomes obscured in curved spacetime, ω in Eq. (39) takes on the meaning of a Lagrange multiplier which minimizes the matter motion with respect to the coordinate system. It only reduces to the orbital angular velocity in the Newtonian (i.e., $r\rightarrow\infty$) limit. Confining orbital motion to the x,y plane, we determine the coordinate rotation frequency ω at each time step from the weighted average of the matter four-velocity and the frame-drag shift vector:

$$\omega=\frac{\int dV(D+\Gamma E)\left[\frac{\alpha(xU_y-yU_x)}{(1+U^2/\phi^4)}-\phi^4(xG_y-yG_x)\right]}{\int dV(D+\Gamma E)(x^2+y^2)}. \tag{42}$$

This rotation is then subtracted from the velocities and added to the coordinate rotation, thereby maintaining a centering of the stars along $y=0$.

The fact that the constraint conditions on (19), (27), and (40) can be written in the form of flat-spaced Poisson equations, allows for these variables to be solved by fast numerical techniques as discussed below. However, their solution requires that boundary values for these variables be specified at distances relatively close to the neutron stars. Our method of determining the boundary values is described in Sec. II F 2.

C. Relativistic hydrodynamics

To solve for the fluid motions of the system in curved spacetime it is convenient to use an Eulerian fluid description [42]. We begin with the perfect fluid stress-energy tensor, which in covariant form can be written

$$T_{\mu\nu}=(\rho+\rho\epsilon+P)U_\mu U_\nu+Pg_{\mu\nu}. \tag{43}$$

By introducing a set of Lorentz-contracted state variables, it is possible to write the relativistic hydrodynamic equations in a form which is reminiscent of their Newtonian counterparts. The hydrodynamic state variables are the coordinate covariant baryon mass density

$$D=W\rho, \tag{44}$$

the internal energy density

$$E=W\rho\epsilon, \tag{45}$$

the three-velocity

$$V^i=\alpha\frac{U_i}{\phi^4 W}-\beta^i, \tag{46}$$

and the momentum density

$$S_i=(D+\Gamma E)U_i, \tag{47}$$

where W is a Lorentz-like factor

$$W=\alpha U^t=\left[1+\sum\frac{U_i^2}{\phi}{}^4\right]^{1/2}, \tag{48}$$

and Γ is an adiabatic index for the equation of state [Eq. (12)].

In terms of these state variables, the hydrodynamic equations are as follows: The equation for the conservation of baryon number takes the form

$$\frac{\partial D}{\partial t}=-6D\frac{\partial\ln\phi}{\partial t}-\frac{1}{\phi^6}\frac{\partial}{\partial x^j}(\phi^6 DV^j). \tag{49}$$

The equation for internal energy conservation becomes

$$\frac{\partial E}{\partial t}=-6\Gamma E\frac{\partial\ln\phi}{\partial t}-\frac{1}{\phi^6}\frac{\partial}{\partial x^j}(\phi^6 EV^j)-P\left[\frac{\partial W}{\partial t}+\frac{W}{\phi^6}\frac{\partial}{\partial x^j}(\phi^6 WV^j)\right]. \tag{50}$$

Momentum conservation takes the form

$$\frac{\partial S_i}{\partial t}=-6S_i\frac{\partial\ln\phi}{\partial t}-\frac{1}{\phi^6}\frac{\partial}{\partial x^j}(\phi^6 S_iV^j)-\alpha\frac{\partial P}{\partial x^i}+2\alpha(D+\Gamma E)\left(W-\frac{1}{W}\right)\frac{\partial\ln\phi}{\partial x^i}+S_j\frac{\partial\beta^j}{\partial x^i}-W(D+\Gamma E)\frac{\partial\alpha}{\partial x^i}-\alpha W(D+\Gamma E)\frac{\partial\chi}{\partial x^i}, \tag{51}$$

where χ is the radiation reaction potential, which is described in Sec. II E. Note that the repeated occurrences of the ϕ^6 factors simply account for proper volume factors [proper volume $=\phi^6(dx^i)^3$]. This is the reason for the choice of conformal scalings introduced in Eqs. (14) and (15). That is, we preserve $\hat{D}$, $\hat{E}$, and $\hat{S}_i$ when ϕ is changed.

Our routines for evolving the hydrodynamics have been previously very well tested at the special relativistic level in [32,43–46], where the hydrodynamics method described here was used to simulate relativistic heavy ion calculations. In that work, shock-wave solutions were compared for both decelerating and accelerating shocks. For the former case, the numerical results were accurate to better than 1% over the range of special relativistic γ factors from 1 to 10, i.e. $E_{\text{thermal}}=0$–$10\ \rho c^2$. For the case of shocks accelerating matter, errors increased to 1% for $\gamma>2$.

A shock-tube calculation was made using a constant adiabatic index of $\Gamma=2$. The density ratio was 100:1, and the initial thermal energy density of the dense matter was equal to the initial baryonic density. The compression ratio of the shocked bow density material was 8% too high. The rest of the density profile was accurate to better than 1%. Relativistic shock-tube solutions were also calculated to test the accuracy of the rarefactions. Again, in the range of interest ($E_{\text{thermal}}\approx\rho c^2$), the overall agreement of numerical results with exact solutions was of order 1%.

On the basis of these results, we anticipate all shocks occurring in the neutron-star coalescence will be treated with sufficient accuracy. Numerical errors are not Lorentz invariant, but tests for invariance have shown that our numerical methods are reliable for changes of frame by a factor of a few in rapidity. In the present work we have extended the hydrodynamics to curved space. However, this extension is straightforward and we do not anticipate any new instability or unacceptable inaccuracy to be introduced thereby. For the calculations described here there is little fluid motion and no strong shock in our rotating frame.

D. Equation of state

For the orbital calculations presented here we use the zero temperature, zero neutrino chemical potential equation of state from the supernova numerical model of Mayle and Wilson [47,48]. While the orbital calculations of concern in this

TABLE I. Zero-temperature equation of state.

ρ (g cm^{-3})	ϵ (erg g^{-1})	P (dyne cm^{-2})	Γ
1.4656×10^{12}	1.1332×10^{19}	4.3839×10^{30}	1.2639
2.1512×10^{12}	1.2429×10^{19}	6.6872×10^{30}	1.2501
3.1575×10^{12}	1.3578×10^{19}	1.0153×10^{31}	1.2368
4.6345×10^{12}	1.4775×10^{19}	1.5364×10^{31}	1.2244
6.8024×10^{12}	1.6016×10^{19}	2.3244×10^{31}	1.2133
9.9847×10^{12}	1.7346×10^{19}	3.6993×10^{31}	1.2136
1.4656×10^{13}	1.8714×10^{19}	5.6944×10^{31}	1.2076
2.1512×10^{13}	2.0241×10^{19}	9.2761×10^{31}	1.2130
3.1575×10^{13}	3.3004×10^{19}	1.0549×10^{32}	1.1012
4.6345×10^{13}	1.2097×10^{19}	8.0239×10^{31}	1.1431
6.8024×10^{13}	1.2750×10^{19}	1.1593×10^{32}	1.1337
9.9847×10^{13}	1.3474×10^{19}	2.2347×10^{32}	1.1661
1.4656×10^{14}	1.4785×10^{19}	6.4224×10^{32}	1.2964
2.1512×10^{14}	1.7477×10^{19}	2.2614×10^{33}	1.6015
3.1575×10^{14}	2.3671×10^{19}	7.0623×10^{33}	1.9449
4.6345×10^{14}	3.5634×10^{19}	1.8609×10^{34}	2.1268
6.8024×10^{14}	5.6410×10^{19}	4.6988×10^{34}	2.2245
9.9847×10^{14}	9.1848×10^{19}	1.1911×10^{35}	2.2988
1.4656×10^{15}	1.5307×10^{20}	3.0204×10^{35}	2.3464
2.2859×10^{15}	2.7681×10^{20}	8.9079×10^{35}	2.4078
3.1575×10^{15}	4.5386×10^{20}	2.1148×10^{36}	2.4757
4.6345×10^{15}	7.7418×10^{20}	4.6612×10^{36}	2.3016
8.1628×10^{15}	1.2080×10^{21}	1.4007×10^{37}	2.1238
9.9847×10^{15}	1.8434×10^{21}	2.0691×10^{37}	2.0865

paper should only involve zero temperature, there is some small shock heating of the stars as they adjust to changing conditions on the grid. Thus, we augment this equation of state with a thermal component (taken to behave as a $\Gamma=5/3$ gas) in order to follow the dynamic evolution equations. Thus, we write

$$P=P_0(\rho)+\tfrac{2}{3}\rho[\epsilon-\epsilon_0(\rho)], \tag{52}$$

where P_0 and ϵ_0 are the zero-temperature pressures and energies.

Table I gives the the zero-temperature values of P_0, ϵ_0, and Γ vs ρ. In Fig. 1 we present the baryonic mass M_B, gravitational mass M_G, the stellar radius in Schwarzschild (r_S) and isotropic (r_I) coordinates, the lapse function α, and the total mass energy density $\rho(1+\epsilon)$ as a function of the central density of an isolated neutron star. From this figure it can be seen that this equation of state gives an upper limit to the gravitational mass of an isolated neutron star of $M_G\leqslant 1.60M_\odot$. (Note that this value supersedes the lower value previously quoted in [34].) This limit roughly agrees with the upper limit of the smallest range of neutron-star masses which overlaps all observational determinations. The fact that this upper limit is close to the typically observed neutron-star mass $M_G\approx 1.45M_\odot$ has important consequences for the examples considered below.

The three-dimensional calculations reported here have only about 15 zones in radius to represent each neutron star. As another test of the accuracy of our three-dimensional calculations, therefore, a hydrodynamic calculation was made of a single star using typical zoning in three dimensions. This

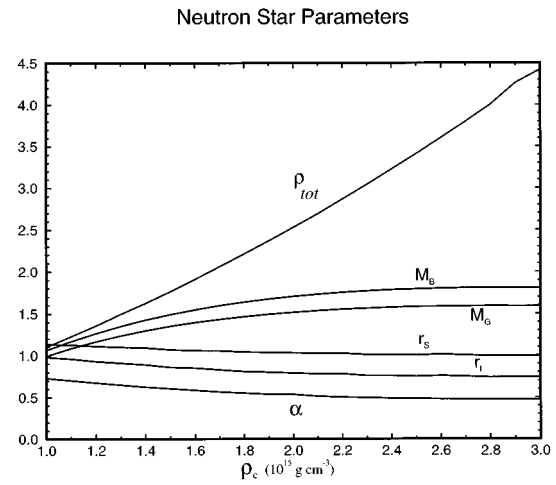

FIG. 1. Various parameters characterizing isolated neutron stars with the adopted equation of state as a function of the central baryon density ρ_c. M_B and M_G are the baryonic and gravitational masses, respectively, in units of $M_\odot$. The radius is given in both Schwarzschild coordinates r_S and in isotropic coordinates r_I in units of 10 km. Also shown are central values for the minimum lapse function α, and the total mass energy density $\rho_{\rm tot}=\rho(1+\epsilon)$ (in units of 10^{15} g cm^{-3}).

calculation was compared with a one-dimensional spherical hydrodynamic calculation with fine zoning. For the same baryonic mass, $1.60M_\odot$, the gravitational masses agreed to 0.7%, i.e., yielding a gravitational mass of $1.45M_\odot$ and $1.46M_\odot$ for the three-dimensional (3D) and 1D calculations, respectively. This we take as indicative of the accuracy of the calculated gravitational binding energy of the binary system as well. Figure 2 shows the density profile for a single isolated $M_G=1.45M_\odot$ neutron star with the adopted equation of state.

E. Gravitational radiation

In general, it is possible to express the emission of gravitational radiation in terms of an ''exact'' expansion of multipole moments of the effective stress-energy tensor, includ-

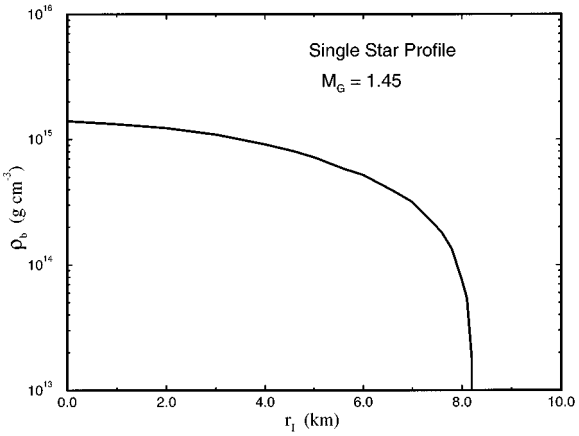

FIG. 2. Density profile as a function of radius (in isotropic coordinates r_I) for an isolated neutron star with a gravitational mass of $1.45M_\odot$.

ing corrections for the so-called ''slow motion'' approximation [41]. It is important to appreciate that these formulas apply to strong-field sources as well as to weak-field sources [49,41] as long as the relevant components of the effective stress-energy tensor can be identified. Since, in the present paper, we are only concerned with orbital motion of equal mass binaries, the multipole expansions reduce to only a few nonzero terms. These we evaluate and test for convergence of the expansion. We summarize below the aspects of [41] which are relevant to our model.

In any coordinate system (such as the one we are using here) in which the gravity waves far from the source can be characterized as linear metric perturbations propagating on a flat background, the transverse traceless part of the metric perturbation characterizes the radiation completely. This metric perturbation can be expressed [41] in terms of the mass multipole (I^{lm}) and current multipole moments (S^{lm}) as

$$h_{jk}^{TT}=\sum_{l=2}^{\infty}\sum_{m=-l}^{l}[r^{-1(l)}I^{lm}(t-r)T_{jk}^{E2,lm} + r^{-1(l)}S^{lm}(t-r)T_{jk}^{B2,lm}], \tag{53}$$

where the superscript TT denotes the transverse traceless part of the metric perturbation and the notations ${}^{(k)}I^{lm}$ and ${}^{(k)}S^{lm}$ denote the kth time derivative of the respective moments.

From this, the general expression for energy loss is

$$\frac{dE}{dt}=\frac{1}{32\pi}\sum_{l=2}^{\infty}\sum_{m=-l}^{l}\langle|{}^{(l+1)}I^{lm}|^2+|{}^{(l+1)}S^{lm}|^2\rangle, \tag{54}$$

where the angular brackets denote averages over several wavelengths. Angular momentum loss can similarly be written

$$\frac{dJ}{dt}=\frac{i}{32\pi}\sum_{l=2}^{\infty}\sum_{m=-l}^{l}\langle{}^{(l)}I^{lm*}m^{(l+1)}I^{lm}\rangle+\langle{}^{(l)}S^{lm*}m^{(l+1)}S^{lm}\rangle, \tag{55}$$

where the expression (55) assumes an alignment of the angular momentum vector with the z axis.

The radiation reaction potential χ for Eq. (51) can be written

$$\chi=\frac{1}{32\pi}\sum_{l=2}^{\infty}\sum_{m=-l}^{l}x_ix_j\langle|{}^{(l+1)}I^{lm}|^2+|{}^{(l+1)}S^{lm}|^2\rangle. \tag{56}$$

Our problem then reduces to the identification of the relevant mass and current moments in our coordinates. For an asymptotically Minkowski coordinate system, one can define a quantity

$$\overline{h}^{\alpha\beta}\equiv-(-g)^{1/2}g^{\alpha\beta}+\eta^{\alpha\beta}, \tag{57}$$

where g is the determinant of the metric and $\eta^{\alpha\beta}$ is the Minkowski metric tensor. If $\overline{h}^{\alpha\beta}$ satisfies the de Donder gauge condition

$$\overline{h}^{\alpha\beta}_{,\beta}=0, \tag{58}$$

then the Einstein field equations take the form

$$\Box\overline{h}^{\alpha\beta}=-16\pi\tau^{\alpha\beta}, \tag{59}$$

where $\tau^{\alpha\beta}$ is the ''effective stress-energy tensor'' [41].

As long as the de Donder condition is valid, Eq. (59) can be inverted (using the flat-space outgoing Green's function) and the Green's function expanded in terms of vacuum basis functions. The resultant expression can then be reduced [41] to provide expansions for the desired mass and current moments:

$$\begin{aligned}I^{lm}=&\frac{16\pi}{(2l+1)!!}\left(\frac{(l+1)(l+2)}{2(l-1)l}\right)^{1/2}\int\tau_{00}Y^{lm*}r^l d^3x\\&+\sum_{k=0}^{\infty}\frac{16\pi}{2^k k!(2l+2k+1)!!}(\partial_t)^{2k}\int\tau_{pq}r^{l+2k}\\&\times\left[\frac{(2l+2k+1)}{2(k+1)}\left(\frac{(l+1)(l+2)}{2(2l-1)(2l+1)}\right)^{1/2}T_{pq}^{2\,l-2,lm*}\right.\\&+\left(\frac{3(l-1)(l+2)}{(2l-1)(2l+3)}\right)^{1/2}T_{pq}^{2\,l,lm*}+\frac{2k}{2l+2k+3}\\&\left.\times\left(\frac{l(l-1)}{2(2l+1)(2l+3)}\right)^{1/2}T_{pq}^{2\,l+2,lm*}\right]d^3x,\end{aligned} \tag{60}$$

and

$$\begin{aligned}S^{lm}=&\frac{-32\pi}{(2l+1)!!}\left(\frac{(l+2)(2l+1)}{2(l-1)(l+1)}\right)^{1/2}\\&\times\int\epsilon_{jpq}x_p(-\tau_{0q})Y_j^{l-1,lm*}r^{l-1}d^3x\\&+\sum_{k=0}^{\infty}\frac{16\pi i}{2^k k!(2l+2k+1)!!}(\partial_t)^{2k+1}\int\tau_{pq}r^{l+2k+1}\\&\times\left[\frac{1}{2(k+1)}\left(\frac{l+2}{2l+1}\right)^{1/2}T_{pq}^{2\,l-1,lm*}\right.\\&\left.+\frac{1}{2l+2k+3}\left(\frac{l-1}{2l+1}\right)^{1/2}T_{pq}^{2\,l+1,lm*}\right]d^3x,\end{aligned} \tag{61}$$

where the Y^{lm*} are the usual spherical harmonics, and $T_{pq}^{2\,l,lm*}$ are the pure-orbital tensor harmonics as defined in [41]. The first integral in Eqs. (60) and (61) is the usual spherical harmonic expansion. At the $l=2$ level, Eq. (60) reduces to the well-known quadrupole approximation. The second integral in Eqs. (60) and (61) is the correction to the slow motion approximation, which is non-negligible in the present application, i.e., $v/c\gtrsim 0.1$.

To evaluate the time derivatives of the mass and current multipole moments we make use of the rotation properties of spherical tensors, whereby rotations can be generated in terms of the Wigner D matrices:

$$I^{lm}=D^{l}_{mm'}I_0^{lm'},\quad S^{lm}=D^{l}_{mm'}S_0^{lm'}, \tag{62}$$

where $I_0^{lm'}$ and $S_0^{lm'}$ are evaluated in the rotating frame. For stable orbits (neglecting gravitational radiation) and hydrostatic stars, these are time-independent quantities.

The main contribution to the time derivatives is that due to orbital motion. Evaluation of the orbital motion reduces to derivatives of the $D^l_{mm'}$ which for our coordinates have a simple $\sim\cos(m\omega t)$ dependence.

The problem with evaluating Eqs. (60) and (61) is that the multipole moments are only defined in the de Donder gauge and not for our conformally flat coordinates. Furthermore, even if the transformation to our coordinates were straightforward (which it is not), the effective stress-energy tensor would not be known.

Fortunately, however, a transformation to the de Donder coordinates is not necessary. It is only necessary that the moments of the metric coordinates be defined in a coordinate system which, such as a de Donder coordinate system, is asymptotically Cartesian and mass centered (ACMC). In [41] it is proved that in such coordinate systems and the covariant metric components are time independent and expandable into a spherical harmonic $(1/r)$ structure in terms of the same moments [i.e., Eqs. (60) and (61)] relevant to the radiation field. Furthermore, these multipole moments are invariant under transformations between two ACMC coordinate systems. From these expansions we can deduce the source for the slow-motion moments to be used in the equations for the radiation field, (54) and (55). For example, the spatial three-metric must obey [41]

$$\gamma_{ij}=\delta_{ij}+\sum_{l=0}^{N}\frac{1}{r^{l+1}}\left[\frac{(2l-1)!!}{2}\left(\frac{2(l-1)l}{(l+1)(l+2)}\right)^{1/2}\times\sum_{m=-l}^{l}I^{lm}Y^{lm}+(l-1\ \text{ pole})+\cdots+(0\ \text{ pole})\right]. \quad (63)$$

On the other hand, our spatial three-metric [Eq. (2)] can also be expanded as the fourth power of a multipole expansion of the flat-space Poisson equation for ϕ [Eq. (19)]:

$$\gamma_{ij}=\phi^4\delta_{ij}=\left[1+\sum_{l=0}^{\infty}\sum_{m=-l}^{l}\frac{4\pi}{(2l+1)}q^{lm}Y^{lm}r^{-(l+1)}\right]^4\delta_{ij}, \quad (64)$$

where

$$q^{lm}=\int d^3x\rho_1(x)r^lY^{lm}*, \quad (65)$$

and ρ_1 is the source term for ϕ [Eq. (20)]. If we collect the dominant linear terms in Eqs. (63) and (64) according to the recipe given in [41], then we can identify the relation between the source ρ_1 for the conformal factor elliptic equation (19) and the mass multipole moments, i.e.,

$$I^{lm}=\frac{32\pi}{(2l+1)!!}\left(\frac{(l+1)(l+2)}{2(l-1)l}\right)^{1/2}q^{lm}. \quad (66)$$

This identification also reduces to the correct Newtonian limit. As can be seen from Eq. (20), $\rho_1\to\rho/2$, where ρ is the Newtonian matter density, so that $\tau_{00}\to\rho$ as required.

TABLE II. Contributions to energy and momentum losses from the orbit calculation with $J=2.7\times10^{11}$ (cm^2).

$\dot{E}_{\rm tot}$ ($M_\odot$ sec^{-1})	6.11×10^{-3}
$\dot{E}_{I22}$	6.32×10^{-3}
$\dot{E}_{\rm SM}$	-2.2×10^{-4}
$\dot{E}_{I44}$	2.0×10^{-7}
$\dot{E}_{S32}$	3.3×10^{-8}
$\dot{E}_{I42}$	2.2×10^{-11}
$\dot{J}_{\rm tot}$ (cm)	1.07
$\dot{J}_{I22}$	1.11
$\dot{J}_{\rm SM}$	-0.034
$\dot{J}_{I44}$	3.6×10^{-5}
$\dot{J}_{S32}$	-5.8×10^{-6}
$\dot{J}_{I42}$	4.2×10^{-9}

The contribution from the current moments is expected to be small as is the slow-motion correction. Therefore, we are mainly concerned with estimating the magnitude of those contributions. To the accuracy desired, we identify the source for the current moments S^{lm} and the slow-motion corrections with the Newtonian-like counterparts, i.e., we set $\tau_{0j}=T_{0j}$, $\tau_{ij}=T_{ij}$. We compute terms out to ω^{10}, which include mass multipoles out to $l=4$, current multipoles out to $l=3$, and the leading correction for the slow-motion correction.

In Table II we summarize the relative contributions of various moments to the energy and angular momentum loss rates. As expected, the quadrupole term dominates. The next largest term is the slow-motion correction which contributes only a few percent to the gravitational radiation and tends to decrease the loss rate.

F. Numerical methods

The elliptic equations for the field and differential evolution equations for the hydrodynamic variables were finite differenced in a Cartesian grid. The intrinsic state variables, $D,W,E,\Gamma,\alpha,\phi,$ are treated as zone-centered quantities, while the four-velocity U_i and momentum densities S_i are node centered. The shift vector β^i and the three-velocity V^i are face centered. After finite differencing, the elliptic equations are reduced to a matrix equation

$$M\cdot x=b, \quad (67)$$

where M is a sparse matrix, x is a vector representing the relevant field variable at each zone, and b is derived from the source terms. This equation can then be solved using any one of a number of fast matrix inversion techniques.

When we solve the elliptic equation for ϕ, the coordinate density D is adjusted so as to preserve the conformal scalings, Eqs. (14) and (15). That is, $\hat{D}=\phi^6D$ is kept constant, which preserves baryon number. Also, the coordinate energy density is changed to preserve $\phi^{6\Gamma}E$ and the momentum density is changed to preserve ϕ^6S^i, which maintains the entropy.

1. Extracting physical observables

The gravitational mass we obtain from the asymptotic behavior of $\phi \to 1+(GM/2r)$ [cf. Eq. (64)]. The angular momentum is more difficult to define. We estimate this from an integral over the spacetime components of the stress-energy tensor [37], neglecting angular momentum in the radiation field:

$$J^{ij}=\int (T^{i0}x^j - T^{j0}x^i)dV. \tag{68}$$

Aligning the z axis with the angular momentum vector then gives

$$J=\int (xS^y - yS^x)dV. \tag{69}$$

2. Boundary conditions

As noted above, our choices for the metric and slicing condition lead to a form for the Hamiltonian and momentum constraints in terms of flat-space elliptic equations, i.e., Eqs. (19), (27), and (40), for the metric variables ϕ, $(\alpha\phi)$, and β^i. A solution to these elliptic equations, however, requires that we specify values for ϕ, $(\alpha\phi)$, and β^i along the outer boundaries of the grid. For a Poisson-like equation, the field variables could be specified by integrating the source function over the interior: e.g.,

$$\phi(x)=\int \frac{\rho_1(x')}{|x-x'|}d^3x'. \tag{70}$$

However, the evaluation of this integral for each point along the boundaries is computationally slow. In principle, an expansion of the source function in spherical harmonics $Y^{lm}(\theta,\phi)$ could be applied to obtain the field variables along the boundaries: e.g.,

$$\phi(x)=1+\sum_{l}^{\infty}\sum_{m=-l}^{l}\frac{4\pi}{2l+1}r^{-(l+1)}q^{lm}Y^{lm}(\theta,\phi). \tag{71}$$

However, the convergence of a spherical harmonic expansion for a source dominated by two separate nearly spherical distributions is quite slow. In order to accommodate these two features, we employ a combination of them which is numerically efficient even at distances relatively close to the neutron stars.

In the equations for ϕ and $(\alpha\phi)$, the boundary values are dominated by contributions from the effective point source potential from each star. Our method of specifying the boundary for ϕ and $(\alpha\phi)$, therefore, is to first make a best fit to the source density, ρ_1 or ρ_2, of each star with a truncated spherical Gaussian profile located at the source-density center of mass in each half of the grid. The boundary values on the computational grid then begin with the sum of the two point-mass contributions from the truncated spherical Gaussian profiles for each star. This provides a simple analytic contribution around the boundary for the bulk of the source.

These Gaussian density profiles are then subtracted from the source density to yield a residual density. An expansion in spherical harmonics up to $l=4$ [Eq. (71)] is then utilized to compute the contribution from the residual source function over the grid. For stars well separated on the grid, this residual source typically accounts for only a few percent of the total boundary value. Also, the spherical harmonic expansion for the residuals converges faster than that for the unsubtracted source function. Hence, a truncation of the expansion to $l=4$ is sufficiently accurate.

A Gaussian source profile turns out to be an excellent approximation in the early stages before the neutron stars begin to coalesce. In future calculations in which the stars will be followed until they merge, however, they will more closely represent a single source function. At some point in the calculation it will become expedient, therefore, to apply the spherical harmonic expansion directly to the unsubtracted source function.

We note that the expansion of the three-metric [Eq. (63)] requires that the asymptotic form for ϕ obeys

$$\phi \to 1+\frac{m_G}{2r}. \tag{72}$$

Similarly, from the ACMC expansion for g_{00} [41], the lapse function must approach

$$\alpha \to 1-\frac{m_G}{r} \tag{73}$$

in order that our time coordinate becomes proper time as $r\to\infty$. The Poisson equation (27) for $(\alpha\phi)$ can also be expanded in spherical harmonics [e.g., Eq. (71)], yielding

$$(\alpha\phi)\to(\alpha\phi)_\infty - \frac{m_{\alpha\phi}}{2r}, \tag{74}$$

where $m_{\alpha\phi}$ is the volume integral over twice the source ρ_2. Since, in general, $m_{\alpha\phi}\neq m_G$, we choose the boundary condition

$$(\alpha\phi)_\infty = \frac{m_{\alpha\phi}}{m_G}, \tag{75}$$

to guarantee that Eq. (73) is satisfied. For the systems studied here, $(\alpha\phi)_\infty \approx 0.98$.

In our computation of the boundary conditions, we impose a spherical cutoff in the matter distributions at a radius equal to the largest sphere that fits within our cubical grid. This avoids the possibility of a spurious hexadecapole moment associated with the cubic grid employed in the calculation. For matter terms this is a reasonable truncation for the calculations presented here, since only a negligible amount of matter appears beyond the surface of the neutron stars. However, the $K_{ij}K^{ij}$ terms in Eqs. (19) and (27) contribute beyond the matter boundary. Also, the shift vector elliptic equations, (37) and (38), involve a source which extends beyond the source boundary.

Regarding the $K_{ij}K^{ij}$ terms we note that these terms are small. For example, the contribution to the gravitational mass from an integration over the interior source function is only $\sim 0.0001 M_\odot$. Furthermore, the asymptotic form for $K_{ij}K^{ij}$ should decay as $1/r^6$. Assuming this form, we estimate that the exterior contribution from the $K_{ij}K^{ij}$ term is $\lesssim 10^{-5}M_\odot$ and can, therefore, be neglected in the examples considered in this paper.

Regarding the solution for the shift vector [Eqs. (37) and (38)], we note that $\nabla \cdot \beta$ is small and changes sign across the grid. This means that the variable χ asymptotically goes to zero. Hence, we impose $\chi = 0$ along the boundary for Eq. (37). A solution for B^i requires that we specify the boundary condition for the ''drag'' component G^i. For this we note that G^i behaves as an angular momentum density and should scale along the boundary as

$$G^x = -\frac{4yJ}{r^3}, \quad G^y = \frac{4xJ}{r^3}. \tag{76}$$

III. ORBIT CALCULATIONS

It is a nontrivial endeavor to find initial configurations for the two neutron stars prior to coalescence. Our method consists of placing two neutron stars on the grid with a rotational velocity sufficient to keep them in orbit and an initial ''guess'' density profile from a solution to the Tolman-Oppenheimer-Volkoff-like equation for two single neutron stars in our isotropic coordinates. The conversion from single star solution to a binary solution is achieved by allowing the stars to relax to an equilibrium configuration on the grid. That is, the field equations are then solved and the hydrodynamics evolved (without the radiation reaction potential and with viscous damping of the fluid motion) until equilibrium is achieved. For the examples to be presented below, we follow the time evolution of the system with constant angular momentum until it has settled down. As the stars settle down the damping is slowly removed.

IV. RESULTS

In this paper we are presenting principally the method of solving the field equations and hydrodynamics for binary neutron stars. As examples, we also discuss below three illustrative calculations made at selected values of the orbital angular momentum with no radiation damping of the orbits. Highlights of these results have been presented previously [34]. Here, we supply more details of the application of the method.

In these calculations the neutron stars are taken to be of equal mass. The baryonic mass was selected so that in isolation each star has a gravitational mass of $1.45 M_\odot$. Although the calculations presented here ignore radiation damping, during most of the evolution the radiation damping is small. Therefore, the stars should follow a sequence of quasiequilibrium configurations which closely match the equilibria computed here. These equilibria can be analyzed to obtain the rates of energy and momentum losses. Ultimately, the implied orbit decay could be used to infer the approximate time evolution through this sequence of quasiequilibrium orbits.

We have placed the stars at various separation distances on the grid and only run the calculation long enough to check whether the system obtains what would be a stable orbit in the absence of gravitational radiation. In total for the three-orbit calculations presented below, we have followed the stars through more than 20 revolutions (with roughly two hours of Cray/YMP CPU time per orbit) to ensure that the orbits have had time to settle down. We have utilized a grid of $100 \times 25 \times 25$ zones for the matter and $100 \times 50 \times 50$ for the field variables. We make use of reflection symmetry in the orbital plane. Also, since here we study equal-mass binaries, we exploit reflection inversion symmetry through the axis joining the centers of the two stars. In effect, this calculation then is equivalent to a three-space grid of 10^6 zones.

TABLE III. Parameters characterizing the orbit calculations at the final edit. M_G is just the total mass of the binary divided by 2.

J (cm^2)	2.2×10^{11}	2.3×10^{11}	2.7×10^{11}
M_B ($M_\odot$)	1.598	1.598	1.598
M_G ($M_\odot$)	1.416	1.420	1.423
f (Hz)	410	310	267
I^{22} (cm^3)	1.19×10^{18}	1.28×10^{18}	2.31×10^{18}
d_I (km)	33.8	34.8	57.0
d_P (km)	39.4	40.6	53.0
$\rho_{\max}$ (g cm^{-3})	2.03×10^{15}	2.70×10^{15}	1.93×10^{15}
$W_{\max}$	1.070	1.090	1.085
$\alpha_{\min}$	0.440	0.379	0.463
$\phi^2_{\max}$	1.90	2.05	1.84
$h \cdot r$ (cm)	1.03×10^{4}	6.76×10^{3}	9.60×10^{3}
$\dot{E}$ ($M_\odot$ sec^{-1})	0.016	0.0040	0.0061
$\dot{J}_{\rm tot}$ (cm)	1.23	0.607	1.07
Orbit	Unstable	Stable	Stable
Stars	Unstable	Unstable	Stable

Initial conditions for two $1.60 M_\odot$ baryonic mass neutron stars were obtained from the isotropic-coordinate form of the Tolman-Oppenheimer-Volkoff hydrostatic equilibrium. Two single-star solutions were then placed on the grid and the hydrodynamic and field equations evolved with viscous damping until a new quasiequilibrium configuration was obtained. In practice, this need only be done once for a selected initial angular momentum. Subsequent orbits are then calculated by perturbing the angular momentum and allowing the system to relax to a new stable configuration (if one exists).

The first calculation was made with an orbital angular momentum of 2.2×10^{11} cm^2. The stars settled down into what appeared at first as a stable orbit, but later (less than one complete orbit) the stars began to slowly spiral in. For this system the angular momentum was not enough to support the orbit. Parameters characterizing this binary at the final time slice calculated are given in Table III. (Note that this table supersedes the table in [35] where lower values were quoted for the central densities.) The stars were followed to a coordinate separation $d_I \approx 34$ km which corresponds to a ratio of proper distance to total isolated mass of the system $m = 2M_G^0$ of $d_p/m = 9.2$, where M_G^0 is the gravitational mass of a single isolated neutron star. By this time it could be concluded that no stable orbit would result. Note that the minimum coordinate light speed α/ϕ^2 is only 0.23 in this case.

Figure 3 shows x,y contours in the $z=0$ plane for the hydrodynamic density D and the metric variables α, and ϕ^2. Countours are drawn for the final time slice calculated, for this angular momentum and the other two cases studied.

We note that even at the last time calculated, the stars are still quite far apart, i.e., the ratio of coordinate separation distance d_I to their single-star radius, $d_I/r_I \gtrsim 4$. Even in a

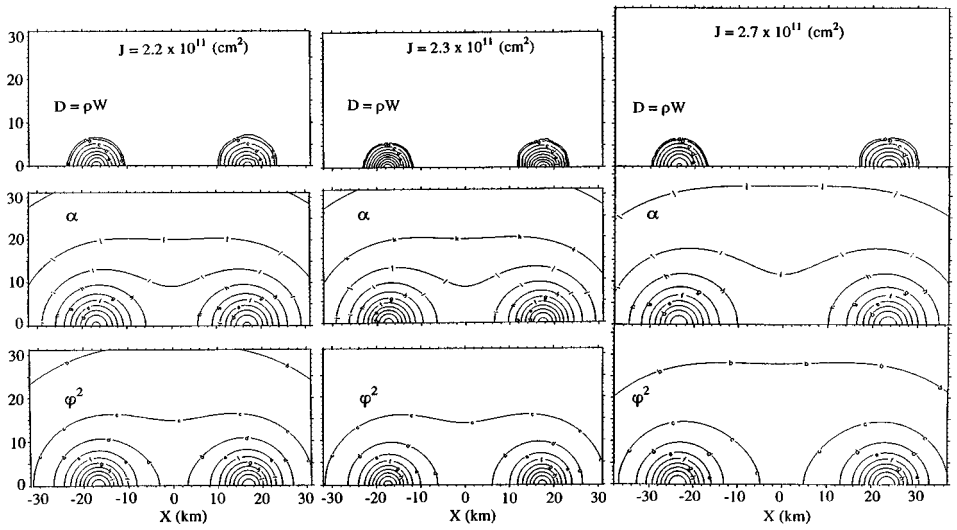

FIG. 3. Contours in the orbit plane for various quantities at the final time slice calculated for $J=2.2\times10^{11}$ cm^2, $J=2.3\times10^{11}$ cm^2, and $J=2.7\times10^{11}$ cm^2 as labeled. The various figures are for coordinate density $D=\rho W$; lapse function α; conformal factor ϕ^2. Note that the $J=2.3\times10^{11}$ cm^2 density contours are more compact illustrating the degree to which these stars have collapsed. See Table III for $\rho_{\max}$, $\phi^2_{\max}$, and $\alpha_{\min}$. Since $W_{\max}=1.09$, $D_{\max}\lesssim\rho_{\max}\times1.09$.

Newtonian hydrodynamic calculation [50], one would expect at most a few percent tidal distortion at this distance. The distortion is made even less, however, by the strong relativistic gravitational field (evidenced in α and ϕ^2 in Fig. 3) around the stars. We also note that the central density increased continuously as the stars spiraled in. The orbit decay time, however, is shorter than the collapse time. Thus, it seems likely that neither the stars nor the orbit are stable for this system as summarized at the bottom of Table III.

The next calculation was made with an angular momentum of 2.3×10^{11} cm^2. The orbit now appeared stable as summarized at the bottom of Table III. However, after about 1–2 revolutions, the central densities were noticed to be rising. By the end of the calculation the central baryonic densities had continuously risen to about 2.7×10^{15} g cm^{-3} ($\approx$10 times nuclear matter density) which is near the maximum density for a stable neutron star (cf. Fig. 1). It appears that neutron stars of this mass range and the adopted equation of state may continue to collapse as long as the released gravitational energy can be dissipated. For this orbit the stars are at a separation distance of $d_p/m=9.5$, far from merging. However, the nonlinearities in the gravitational field have pushed the stars over the critical density for forming a black hole. By the time the calculation was ended, the minimum α had diminished to 0.379 and ϕ^2 risen to 2.05, corresponding to a minimum light speed of 0.18. Figure 3 shows the stars as somewhat more compact objects which are continuing to collapse.

The final calculation was made with the angular momentum increased to 2.7×10^{11} cm^2. As can be seen in Table III and Fig. 3, the stars at this separation $d_p/m=12.4$ appear both stable and in a stable orbit. Note that even for this distance, the gravitational field (α and ϕ) remains strong.

Figure 4 shows vector fields for U_x,U_y, V_x,V_y, and β_x,β_y for the calculation with $J=2.3\times10^{11}$ cm^2. Figures for the other two runs look quite similar. The maximum value of the covariant velocity is $|U_x,U_y|=0.9$. The contravariant three-velocities show the net fluid motion after subtraction of the orbital motion. The maximum magnitude is $|V_x,V_y|=0.07$. We note that even in the corotating frame, V_x,V_y exhibits some rotation. Although the stars are initially corotating, as the stars relax to their equilibrium orbit, they acquire net rotation relative to the orbital motion. The net fluid motion is still much greater than the collapse velocity which is more than an order of magnitude slower than the

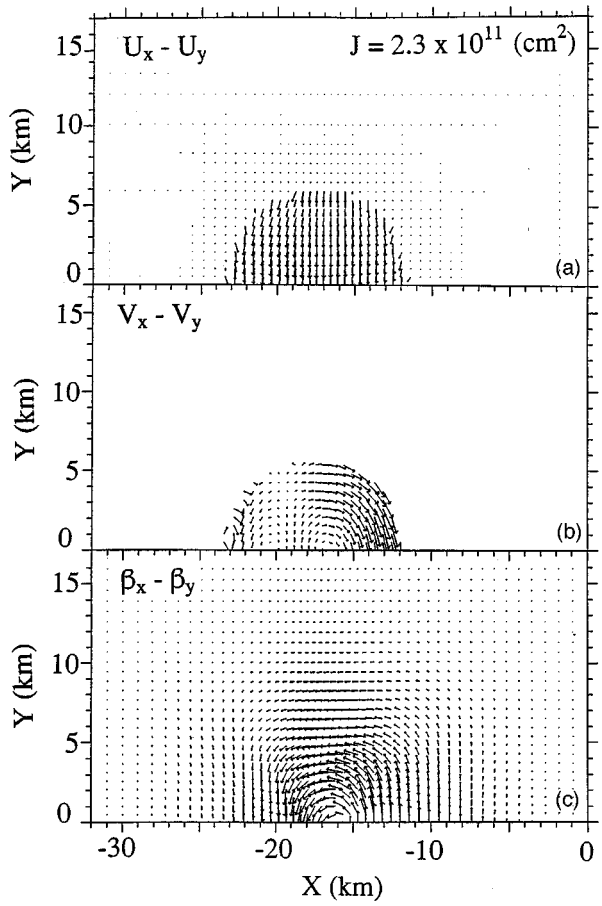

FIG. 4. Vectors in the x,y orbit plane around the star centered at $x=-17.4$ km. This is at the final time calculated for the binary with $J=2.3\times10^{11}$ cm^2. The various figures are for: (a) four-velocity U_x,U_y (showing the overall orbit motion); (b) the rotation subtracted contravariant three-velocity V^x,V^y (showing the corotation and collapse of the fluid); and (c) the rotation-subtracted shift vectors β_x,β_y (showing the relativistic frame drag around the star).

maximum vector shown here. A peculiar aspect of the velocity field in the rotating frame is that the fluid appears to be circulating about a vorticity which does not coincide with the central extrema in density or field variables. It also appears that the parts of the stars most distant from the companion rotate in an opposite sense, generating a second vorticity. The shift vectors are also plotted with the rotation subtracted. What remains is frame drag around the star due to its rotation which has a maximum amplitude of 0.015. It is also slightly offset from the centers of the stars.

A. Analysis of the collapse instability

Having observed the collapse instability numerically in the neutron-star binary, one, of course, would like to have at least a qualitative understanding of the source of this deviation from Newtonian intuition. Here, we present a heuristic explanation of the observed increase in density as the stars approach each other. We trace this increase to the effects of the Lorentz-like factor W^2-1. This factor accounts for the specific kinetic energy of the orbital motion of the stars. Its effect is to increase the effective source strength.

From Eq. (13) the Hamiltonian density ρ_H has a term $(W^2-1)(\rho+\rho\epsilon\Gamma)$ which enters into the source term ρ_1 for ϕ. Similarly, the source for the Poisson equation for $(\alpha\phi)$ [cf. Eq. (26)] has a term $(W^2-1)\times 3(\rho+\rho\epsilon\Gamma)$. Thus, the source terms for both ϕ and α will increase as the separation distance decreases and W exceeds unity. A stronger source term will imply larger values for both ϕ and α at the centers of the stars and therefore steeper gradients of these quantities as one moves outward from the center of each star.

In isotropic coordinates, the general relativistic condition of hydrostatic equilibrium for each star can be inferred from the dominant terms in the momentum equation (51),

$$\frac{\partial P}{\partial x^i}=-(\rho+\rho\epsilon\Gamma)\left(\frac{\partial \ln\alpha}{\partial x^i}+\left[\frac{\partial \ln\alpha}{\partial x^i}-2\frac{\partial \ln\phi}{\partial x^i}\right](W^2-1)\right), \tag{77}$$

where we have ignored the centrifugal term, $S_j(\partial\beta^j/\partial x^i)$. From this we see that the effective gravitational force [right-hand side of Eq. (77)] increases both because (W^2-1) exceeds unity and because the gradients of α and ϕ are more steep as W^2 increases. A further increase of binding arises from the $K^{ij}K_{ij}$ terms in the field sources, but these terms are much smaller than the W^2-1 contributions.

In our rotating coordinate system, the fluid three-velocities V^i are nearly zero. Hence, from Eq. (46) we have

$$W^2-1=\frac{1}{(\alpha^2/\omega^2R^2\phi^4)-1}, \tag{78}$$

where R is the distance from the center of mass. Along the line between centers in the $J=2.3\times10^{11}$ cm^2 model, an effective velocity of $(\omega R\phi^2/\alpha)=0.28$ is obtained. In the stars the average value is $(W^2-1)\sim$ 5–10%. Including both the α and ϕ terms in Eq. (77), we then estimate that the effective hydrostatic gravitational force on the stars is increased by 10–20% over that of stationary nonorbiting stars for which $(W^2-1)=0$. This increased gravitational attraction is sufficient to induce the calculated increase of central densities as the stars approach one another. An important ingredient in this analysis, however, is that we have assumed zero-thermal energy as the stars collapse, that is, we have assumed that neutrino emission is efficient enough to radiate away the released gravitational binding energy so that the stars remain effectively cold.

B. Comparison with post-Newtonian results

Much of the early evolution of a neutron-star binary should be describable with post-Newtonian techniques. However, one desires an understanding of where in the evolution the post-Newtonian approximation diverges from a fully relativistic treatment. For this reason it is of interest to compare the results here with those obtained by a post-Newtonian treatment. We caution, however, that such a comparison is ambiguous. The two formalisms invoke different gauge choices. Hence, parameters can have different meanings.

Our intermediate orbit ($J=2.3\times10^{11}$ cm^2) appears to be on the verge of the transition from steady inspiral to unstable plunge. Therefore, it is convenient to compare these results with the (post)$^{5/2}$-Newtonian analysis of this transition in an equal mass binary as given in Ref. [22]. In that paper a search was made for the innermost stable circular orbit in the absence of radiation-reaction terms in the equations of motion. This is analogous to the calculations performed here which also have analyzed orbit stability in the absence of radiation reaction.

In the (post)$^{5/2}$-Newtonian equations of motion, a circular orbit is derived by setting time derivatives of the separation, angular frequency, and the radial acceleration to zero. This leads to the circular orbit condition [22]

$$\omega_0^2=mA_0/d_h^3, \tag{79}$$

where ω_0 is the circular orbit frequency, $m=2M_G^0$, d_h is the separation in harmonic coordinates, and A_0 is a relative acceleration parameter which for equal mass stars becomes

$$A_0=1-\frac{3}{2}\frac{m}{d_h}\left[3-\frac{77}{8}\frac{m}{d_h}+(\omega_0 d_h)^2\right]+\frac{9}{4}(\omega_0 d_h)^2. \tag{80}$$

Equations (79) and (80) can be solved to find the orbit angular frequency as a function of harmonic separation d_h. The gravity wave frequency is then twice the orbit frequency, $f=\omega_0/\pi$.

Figure 5 shows the circular orbit post-Newtonian gravity wave frequency vs separation distance compared with the present numerical calculations. A striking feature of the present work is that as the stars approach one another, the frequency becomes nearly independent of the separation distance until the orbit becomes unstable to plunge at a relatively large separation.

The main parameter characterizing the last stable orbit in the post-Newtonian calculation is the ratio of coordinate separation to total mass (in isolation) d_h/m. The analogous quantity in our nonperturbative calculation is proper separation to gravitational mass, d_P/m. The separation corresponding to the last stable orbit in the post-Newtonian analysis does not occur until the stars have approached 6.03 m. For $M_G^0=1.45M_\odot$ stars this would correspond to a separation

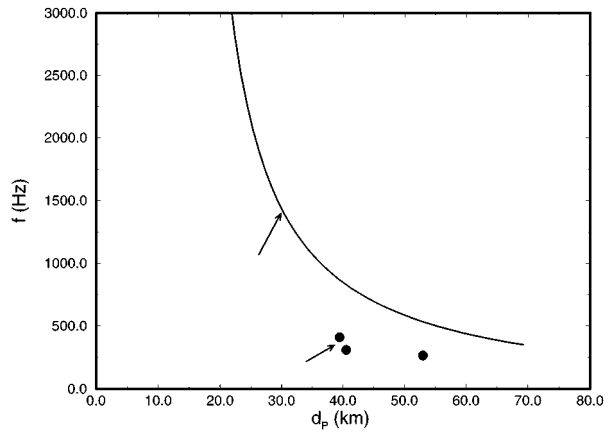

FIG. 5. Comparison of gravity-wave frequency f vs proper separation distance d_P from the present work (points) and post-Newtonian circular orbit condition (line). The arrows show approximate locations of the last stable circular orbit in the two schemes.

distance of about 26 km. In the results reported here, however, the last stable orbit occurs somewhere just below 9.4 m_G^0 at a proper separation distance of $d_P \approx 40$ km.

The fact that we observe the last stable orbit to occur at a larger separation is consistent with the results of Wex and Schäfer [23], who found that higher-order post-Newtonian terms beyond those considered in [22] were significant. They found an unstable orbit at 7.50 m with a large possible uncertainty. A larger separation is also consistent with the numerical initial-data calculation for two black holes by Cook [51]. In that paper a minimum proper separation between *horizon's* of 4.88 m was found. If the black hole results were naively applied to the curved space around the two neutron stars by adding this distance to their Schwarzschild radii, this would correspond to a separation of 8.88 m between centers.

The difference in $J/2M_G^0\mu^0$ also reflects this larger distance. Note, however, that even though the stars are much farther apart, the relativistic treatment gives a stronger gravitational binding energy for this system. However, our binding energy includes the increased self-binding of the individual stars.

Given that the separation distance is greater and that $\omega \sim r^{3/2}$, we would observe a frequency which is a factor of $(40/26)^{3/2} \approx 2$ slower than the post-Newtonian estimates if separation distance were the only relevant effect. However, our angular frequency is about a factor of 2 less than the post-Newtonian value even at the same separation distance. We can understand this nonlinear effect of general relativity heuristically. This difference in orbit frequency should trace to the balance between the gravitational and centripetal forces. From the momentum equation (51) with $W=1$ we can write the dominant terms as

$$(D+\Gamma E)\frac{\partial \ln\alpha}{\partial x^i} = S_j \frac{\partial \beta^j}{\partial x^i}. \tag{81}$$

The left-hand side is the analogue of the Newtonian gravitational force. The right-hand side is the analogue of the centripetal force.

Along the $y=0$ axis we have $\beta^y \approx \omega x$ and $S_y = (D+\Gamma E)U_y$. Thus, we may write

$$\frac{\partial \ln\alpha}{\partial x} = \omega U_y. \tag{82}$$

Taking the fluid three-velocities in the rotating frame to be zero, $V^i=0$, then, from Eq. (46),

$$U_y = \frac{\omega x \phi^4}{\alpha^2\sqrt{1-\omega^2\phi^4x^2}}. \tag{83}$$

Hence,

$$\frac{\partial \ln\alpha}{\partial x} = \omega^2 x \frac{\phi^4}{\alpha^2\sqrt{1-\omega^2\phi^4x^2}}. \tag{84}$$

From this we see that the analogue of the Newtonian centripetal term is enhanced by a factor of $\phi^4/(\alpha^2\sqrt{1-\omega^2\phi^4x^2})$. The average of this quantity along a line joining the centers of the stars is ≈ 7.0. Thus, a much smaller value for the orbital frequency ω provides a sufficient centripetal force to maintain a stable orbit.

V. CONCLUSION

We have summarized a method to study the relativistic evolution of a binary neutron-star system. We have illustrated the method by following the evolution of a close binary through several orbits for different angular momenta in the absence of radiation reaction. These results show two new results which to our knowledge have not been reported previously.

One significant aspect of these calculations is that the binary orbit becomes unstable at a much larger separation distance (a factor of ≈ 1.6) than that derived from $(\text{post})^{5/2}$-Newtonian analysis. This implies that the nonlinear effects of gravity become important much earlier on, and that searches for gravity waves may observe the final merger to occur at a lower frequency than expected. This is important, since it places the coalescence closer to the maximum sensitivity range of the LIGO detector and others. However, we estimate little tidal distortion or hydrodynamic amplification of the the gravity-wave signal. Our estimate of the gravity-wave amplitude near the final orbit is $h \approx 3\times 10^{-23}$ (at 100 Mpc), (see Table II for a summary of the gravitational wave information).

A second significant result of the present calculation is that the nonlinear effects of the fully relativistic gravity imply deep gravitational wells as two neutron stars approach each other. Indeed, the fields can become so strong that the stars are *individually* unstable to collapse into two black holes. Exactly when or if this instability occurs is of course dependent upon the (EOS equation of state). However, for the realistic EOS employed here, this collapse is observed to occur while the stars are still in a quasistable orbit. This suggests that there could be many orbits after black-hole formation until the stars actually merge as two black holes. If correct, this result will have a significant impact on future studies of binary neutron-star mergers and renders the two-black-hole coalescence much more important. Furthermore, the possibility of a collapse many orbit periods before coalescence may have observational consequences not only for

gravity-wave detectors, but in electromagnetic (optical, radio, x-ray and γ-ray bursts) signals as well. We note that even for our unstable inner orbit, the specific angular momentum $a=J/M_G^2\approx 1.3$ is greater than unity, implying that more angular momentum must be lost before merger can occur, although a transient black hole may be able to form with $a>1$.

The importance of the possibility of premerger stellar collapse is dependent on the equation of state and the distribution of neutron star masses. As stated earlier, the EOS we use is the same one used by Mayle and Wilson [47,48] in their supernova model. Calculations made with this EOS for a model of supernova 1987A give an explosion energy of 1.5×10^{51} ergs, consistent with observation. Also, the neutrino spectra and time of neutrino emission are in good agreement with the IMB and Kamiokande neutrino detections [52]. These models also give a good reproduction of heavy element nucleosynthesis in the baryon wind from the proto-neutron star [53]. An important point is that with a stiffer EOS (which would allow a higher-mass neutron star), Mayle and Wilson were not able to obtain satisfactory results.

Regarding, the upper mass limit to neutron stars from observations, Finn [54] has recently analyzed the observed masses of neutron stars and has assigned a lower limit of $1.15-1.35M_\odot$ and an upper limit of $1.44-1.50M_\odot$ at the 1σ (68%) confidence level. At the 2σ (95%) confidence level the upper limit only increases to $1.43-1.64M_\odot$. In an independent approach, Bethe and Brown [55] have recently argued from nucleosynthesis constraints that the maximum neutron star mass is $1.56M\odot$. They also point out that if kaon condensation is taken into account the critical mass may only be $1.50M_\odot$. As seen in Fig. 1, our upper mass limit is $1.60M_\odot$ and the mass of the stars in our sample calculations is $1.45M_\odot$, quite consistent with the observational limits. If the maximum observed stellar mass was as low as the 1σ upper limit, i.e., $1.50M_\odot$, it could be that almost all neutron-star binaries would precollapse before coalescence.

The sample calculations presented here were made with a relatively coarse spatial zoning (see Sec. II D). We, therefore, consider the present results to be only qualitatively correct. They must be supplemented with more detailed numerical modeling. We are presently developing methods for improved numerical efficiency so that results will be of sufficient accuracy to allow for a quantitative interpretation of future observed neutron-star binary collapse and coalescence.

Note that for the above examples, $\dot{J}/\omega J\approx 10^{-4}$ justifyies our neglect of gravitational radiation. Also, we point out that since this paper was submitted it has come to our attention that a study has been made [56] of the validity of the conformally flat condition when applied to rapidly rotating isolated neutron stars. This is the simplest case for which the conformal approximation is different from the exact equations. This work is encouraging in that it has shown that the method works remarkably well.

From the above discussion it is clear that further studies are warranted, particularly an effort to better determine the last stable orbit and the approach to this orbit, as well as a systematic study of the sensitivity of the collapse instability to the neutron-star EOS. Work along this line is currently in progress. There is also a need to investigate orbits at larger radii so that a reliable connection to calculations in the post-Newtonian regime can be made. Once this is done, one can combine the post-Newtonian and numerical (3+1) results to produce a template of expected gravity-wave signals. These can then be used to better extract the gravity-wave signal from the noise.

ACKNOWLEDGMENTS

We gratefully acknowledge contributions from S. L. Detweiler and C. R. Evans who helped us with the derivation of the field equations and moment expansion. We also acknowledge contributions from Hannu Kurki-Suonio who helped us with some of the code development. Helpful conversations with D. Eardley and R. V. Wagoner are also gratefully acknowledged. This work was performed in part under the auspices of the U.S. Department of Energy by the Lawrence Livermore National Laboratory under Contract No. W-7405-ENG-48 and under NSF Grant No. PHY-9401636. The work at the University of Notre Dame was supported in part by U.S. DOE Nuclear Theory Grant No. DE-FG02-95ER40934.

[1] R. A. Hulse and J. H. Taylor, Astrophys. J. **195**, L51 (1975).
[2] G. H. Stokes, J. H. Taylor, and R. J. Dewey, Astrophys. J. **294**, L21 (1985).
[3] S. B. Anderson, P. W. Gorham, S. R. Kulkarni, T. A. Prince, and A. Wolszczan, Nature (London) **346**, 42 (1990).
[4] A. Wolszczan, Nature (London) **350**, 688 (1991).
[5] J. P. A. Clark and D. M. Eardley, Astrophys. J. **215**, 311 (1977).
[6] J. P. A. Clark, E. P. J. van den Heuvel, and W. Sutantyo, Astron. Astrophys. **72**, 120 (1979).
[7] K. Thorne, in *300 Years of Gravitation*, edited by S. Hawking and W. Israel (Cambridge University Press, Cambridge, England, 1984), p. 378.
[8] B. F. Schutz, Nature (London) **323**, 310 (1986).
[9] B. F. Schutz, Class. Quantum Grav. **6**, 1761 (1989).
[10] C. Cutler *et al.*, Phys. Rev. Lett. **70**, 2984 (1993).
[11] E. Amaldi *et al.*, Astron. Astrophys. **216**, 325 (1989).
[12] A. Abramovici *et al.*, Science **256**, 325 (1992).
[13] C. Bradaschia *et al.*, Nucl. Instrum. Method Phys. Res. Sect. A **289**, 518 (1990).
[14] R. Narayan, T. Piran, and A. Shemi, Astrophys. J. **379**, L17 (1991).
[15] E. S. Phinney, Astrophys. J. **380**, L17 (1991).
[16] B. Paczyński, Astrophys. J. Lett. **308**, L43 (1986).
[17] B. Paczyński, Astrophys. J. **363**, 218 (1990).
[18] T. Piran, Astrophys. J. Lett. **389**, L45 (1992).
[19] E. Symbalisty and D. N. Schramm, Astrophys. Lett. **22**, 143 (1982).

[20] B. S. Meyer, Astrophys. J. **343**, 254 (1989).
[21] C. W. Lincoln and C. M. Will, Phys. Rev. D **42**, 1123 (1990).
[22] L. E. Kidder, C. M. Will, and A. G. Wiseman, Phys. Rev. D **47**, 3281 (1993).
[23] N. Wex and G. Schäfer, Class. Quantum. Grav. **10**, 2729 (1993).
[24] F. A. Rasio and S. L. Shapiro, Astrophys. J. **401**, 226 (1992).
[25] M. B. Davies, W. Benz, T. Piran, and F.-K. Thielemann, Astrophys. J. **431**, 742 (1994).
[26] K. Oohara and T. Nakamura, Prog. Theor. Phys. **82**, 535 (1989).
[27] K. Oohara and T. Nakamura, Prog. Theor. Phys. **83**, 906 (1990).
[28] T. Nakamura and K. Oohara, Prog. Theor. Phys. **82**, 1066 (1989).
[29] M. Ruffert, H. T. Janka, and G. Schafer, Astrophys. Space Sci. **231**, 423 (1995).
[30] G. J. Mathews, C. R. Evans, and J. R. Wilson, in *Advances in Nuclear Astrophysics*, edited by E. Vangioni *et al.* (Editions Frontières, Gif-sur-Yvette, France, 1986), p. 211.
[31] G. J. Mathews, J. R. Wilson, C. R. Evans, and S. L. Detweiler, in *Proceedings of the Texas A&M Symposium on Hot Nuclei*, College Station, Texas, 1987, edited by S. Shlomo *et al.* (World Scientific, Singapore, 1988), p. 24.
[32] J. R. Wilson and G. J. Mathews, in *Frontiers in Numerical Relativity*, edited by Evans *et al.* (World Scientific, Singapore, 1989), p. 306.
[33] J. R. Wilson and G. J. Mathews, in *General Relativity*, Proceedings of the 7th Marcel Grossman Meeting on General Relativity, Stanford, California, 1994, edited by A. Ruffini and M. Keiser (World Scientific, Singapore, 1995).
[34] J. R. Wilson and G. J. Mathews, Phys. Rev. Lett. **75**, 4161 (1995).
[35] G. J. Mathews and J. R. Wilson, in *Proceedings of the 3rd Huntsville Gamma Ray Burst Symposium*, 1995 (AIP, New York, in press).
[36] R. Arnowitt, S. Deser, and C. W. Misner, in *Gravitation*, edited by L. Witten (Wiley, New York, 1962), p. 227.
[37] C. W. Misner, K. S. Thorne, and J. A. Wheeler, *Gravitation* (Freeman, San Francisco, 1973).
[38] C. R. Evans, Ph.D. thesis, University of Texas, 1985.
[39] P. Anninos, D. Hobill, E. Seidel, and L. Smarr, Phys. Rev. Lett. **71**, 2851 (1993).
[40] J. W. York, Jr., in *Sources of Gravitational Radiation*, edited by L. Smarr (Cambridge University Press, Cambridge, England, 1979), p. 83.
[41] K. S. Thorne, Rev. Mod. Phys. **52**, 299 (1980).
[42] J. R. Wilson, in *Graviation* [37], p. 423.
[43] J. R. Wilson, T. L. McAbee, and C. T. Alonso, Int. J. Mod. Phys. A **5**, 543 (1990).
[44] J. A. Zingman, R. L. McAbee, J. R. Wilson, and C. T. Alonso Phys. Rev. C **38**, 760 (1988).
[45] T. L. McAbee, J. R. Wilson, J. A. Zingman, and C. T. Alonso Mod. Phys. Lett. A **4**, 983 (1989).
[46] T. L. McAbee and J. R. Wilson, Nucl. Phys. **A576**, 626 (1994).
[47] R. W. Mayle, M. Tavani, and J. R. Wilson, Astrophys. J. **418**, 398 (1993).
[48] James R. Wilson and Ronald W. Mayle, Phys. Rep. **227**, 97 (1993).
[49] W. H. Press and K. S. Thorne, Annu. Rev. Astron. Astrophys. **10**, 335 (1972).
[50] D. Lai, F. A. Rasio, and S. L. Shapiro, Astrophys. J. **420**, 811 (1994).
[51] G. B. Cook, Phys. Rev. D **50**, 5015 (1994).
[52] R. M. Bionata, Phys. Rev. Lett. **58**, **1494 (**1987); K. Hirata, *ibid.* **58**, 1490 (1987).
[53] S. E. Woosley *et al.*, Astrophys. J. **433**, 229 (1994).
[54] L. S. Finn, Phys. Rev. Lett. **73**, 1878 (1994).
[55] H. A. Bethe and G. E. Brown, Astrophys. J. **445**, L129 (1995).
[56] G. B. Cook, S. L. Shapiro, and S. A Teukolsky, Phys. Rev. D **53**, 5533 (1996).